

## Article

# Tuning the Hardness of Produced Parts by Adjusting the Cooling Rate during Laser-Based Powder Bed Fusion of AlSi10Mg by Adapting the Process Parameters

Artur Leis <sup>1,2,\*</sup> , David Traunecker <sup>1</sup>, Rudolf Weber <sup>1</sup> and Thomas Graf <sup>1</sup> <sup>1</sup> Institut für Strahlwerkzeuge (IFSW), Pfaffenwaldring 43, 70569 Stuttgart, Germany<sup>2</sup> Graduate School of Excellence advanced Manufacturing Engineering (GSeME), Nobelstraße 12, 70569 Stuttgart, Germany

\* Correspondence: artur.leis@ifsw.uni-stuttgart.de; Tel.: +49-(0)711-685-60428

**Abstract:** The mechanical properties of parts produced by laser-based powder bed fusion (LPBF) are mainly determined by the grain structure in the material, which is governed by the cooling rate during solidification. This cooling rate strongly depends on the scan velocity and the absorbed laser power. Experiments with varying process parameters were performed to develop and validate an analytical model that predicts the hardness of printed AlSi10Mg parts. It was found that it is possible to tune the hardness of additively manufactured parts of AlSi10Mg in a range between  $60 \pm 9$  HV0.5 and  $100 \pm 10$  HV0.5 by adjusting the cooling rate during solidification with adapted process parameters.

**Keywords:** LPBF; additive manufacturing; hardness; mechanical properties; AlSi10Mg



**Citation:** Leis, A.; Traunecker, D.; Weber, R.; Graf, T. Tuning the Hardness of Produced Parts by Adjusting the Cooling Rate during Laser-Based Powder Bed Fusion of AlSi10Mg by Adapting the Process Parameters. *Metals* **2022**, *12*, 2000. <https://doi.org/10.3390/met12122000>

Academic Editor: Hao Zhou

Received: 27 October 2022

Accepted: 19 November 2022

Published: 22 November 2022

**Publisher's Note:** MDPI stays neutral with regard to jurisdictional claims in published maps and institutional affiliations.



**Copyright:** © 2022 by the authors. Licensee MDPI, Basel, Switzerland. This article is an open access article distributed under the terms and conditions of the Creative Commons Attribution (CC BY) license (<https://creativecommons.org/licenses/by/4.0/>).

## 1. Introduction

The large variety of process parameters used for laser-based powder bed fusion (LPBF) allows for the individual production of parts with a wide range of specific properties. However, the parameters are commonly optimized to only achieve parts with high density and usually not with respect to mechanical properties. Strategies to enhance the quality of the manufactured parts have been summarized by Ravalji and Raval [1]. Investigations of the influence of curved surfaces of additively manufactured parts have shown that geometry has a significant influence on high-cycle fatigue properties [2]. Geometrical optimization [3] and multi-material approaches [4] have been presented to yield tailored, lightweight and mechanical properties of components produced by LPBF. Since the mechanical properties of the produced parts are only insufficiently predictable with the present state of knowledge, the majority of additively manufactured parts are post-processed by heat treatment [5,6].

The mechanical properties of the parts printed by LPBF are largely determined by the cooling rate during solidification, which influences the grain structure of the material [7,8]. High cooling rates lead to smaller grain sizes [7,8]. The influence of the grain size on mechanical properties is described by the Hall-Petch relationship, which states that a decrease of grain size leads to an increased yield strength of the material [9], which in turn is proportional to the hardness [10–13]. The application of the Hall-Petch relationship has been shown for LPBF-manufactured stainless steel 316L, high nitrogen steel, maraging steel 300, and CuNiSi [14]. The influence of the process parameters on the grain size has not been investigated. Esmailizadeh et al. [15] presented an investigation of the influence of the scan velocity of the laser beam on the mechanical properties of Hastelloy X with otherwise constant parameters. It was found that the mechanical properties were improved with increasing scan velocity. The investigation of the mechanical properties as a function of grain size showed a good agreement with the Hall-Petch relationship.

The influence of the process parameters on absorptance plays a major role in the interaction between the laser beam and the processed material, and has already been investigated for AlSi10Mg and other materials suitable for LPBF [16–21].

The influence of the incident laser power  $P_L$  and the scan velocity  $v$  of the laser beam on the resulting mechanical properties of parts made of AlSi10Mg remains the subject of investigations.

Therefore, the present study reports on the determination of the influence of  $P_L$  and  $v$  on the cooling rate, and hence, the resulting hardness. The process parameters used in the experiments covered the full optimum process window given by  $2000 \text{ W/mm} < P_L/d_b < 5200 \text{ W/mm}$ , where  $P_L$  is the incident laser power and  $d_b$  is the diameter of the laser beam on the surface of the workpiece, and were limited to dimensionless Péclet numbers of  $Pe = (d_b \cdot v)/\kappa \leq 16/\pi$  to match the case of three-dimensional heat flow [22–24]; where  $\kappa = \lambda_{th}/(\rho \cdot c_p)$  is the temperature conductivity,  $\lambda_{th}$  is the thermal conductivity,  $\rho$  is the density, and  $c_p$  is the specific heat capacity of the material. Within these constraints, the cooling rate of the processed bead of AlSi10Mg-parts generated by LPBF and the resulting hardness is tunable by varying  $P_L$  and  $v$ .

In the following sections, we first introduce the theory and then describe the experimental setup, as well as the generation, preparation, and analysis of the samples, after which the influence of the process parameters on the cooling rate and the hardness of the parts is presented. Finally, a discussion of the results extrapolates how the hardness of additively manufactured AlSi10Mg parts can be tuned by adjusting the cooling rate with properly adapted process parameters.

## 2. Theory

The Vickers hardness

$$HV = k \cdot \sigma_y \quad (1)$$

of aluminium and aluminium alloys is proportional to the yield strength  $\sigma_y$ , with the proportionality factor  $k$  ranging between  $2.49^{-1}$  and  $2.74^{-1}$  [10,11]. According to the Hall-Petch-Relationship [9], the yield strength is given by

$$\sigma_y = \sigma_0 + \frac{C}{\sqrt{d_c}}, \quad (2)$$

where  $\sigma_0 \approx 35 \text{ N/mm}^2$  is the yield strength of the single crystal of aluminium,  $C$  is the resistance of the grain boundary ranging between 60 and  $280 \frac{\text{N} \cdot \sqrt{\mu\text{m}}}{\text{mm}^2}$  [25–28], which will be used as a fit-factor  $C_{fit}$  in the following, and  $d_c$  is the diameter of the grain size [9]. The grain size

$$d_c = d_{SDAS} = K_{HP} \cdot (-\dot{T})^{-n} \quad (3)$$

can be expressed by the secondary dendrite arm spacing  $d_{SDAS}$  [7,29,30] and is a function of the cooling rate  $-\dot{T}$ , where  $K_{HP} = 165 \mu\text{m} \frac{\text{s}^{-n}}{\text{K}^{-n}}$  and  $n = 0.4$  for the used aluminium alloy AlSi10Mg [8].

Inserting Equations (3) and (2) with  $C = C_{fit}$  in Equation (1) yields the Vickers hardness

$$HV(\dot{T}) = k \cdot \left( \sigma_0 + \frac{C_{fit}}{\sqrt{K_{HP} \cdot (-\dot{T})^{-n}}} \right) \quad (4)$$

as a function of the cooling rate  $-\dot{T}$ .

The diameter of the moving laser beam used in LPBF typically ranges between 25 and 200  $\mu\text{m}$ . Taking this, the spatial extent of the considered volume, and the low Péclet numbers into account, the heat flow during the LPBF process may be modeled by solving the three-dimensional heat-conduction equation for a point source moving in positive

$x$ -direction on the surface of a semi-infinite body [31,32]. With the origin of the coordinate system at the location of the point source, the resulting temperature

$$T(z = y = 0, x < 0) = -\frac{\eta_{Abs} \cdot P_L}{2 \cdot \pi \cdot \lambda_{th} \cdot x} + T_{amb} \quad (5)$$

on the irradiated surface ( $z = 0$ ) along the beam path ( $y = 0$ ) behind the moving point source ( $x < 0$ ) is a function of the absorbed laser power  $\eta_{Abs} \cdot P_L$ , the thermal conductivity  $\lambda_{th}$ , and the distance  $x$  from the point source [31,32], where  $\eta_{Abs}$  is the absorptance in the interaction zone and  $T_{amb}$  is the ambient temperature as given by the pre-heating of the substrate.

Therefore, the location of solidification behind the heat source is given by

$$x_{sol} = -\frac{\eta_{Abs} \cdot P_L}{2 \cdot \pi \cdot \lambda_{th} \cdot (T_{sol} - T_{amb})} \quad (6)$$

where  $T_{sol}$  is the solidification temperature of the processed material.

The differentiation of Equation (5) yields the temperature gradient

$$\frac{\partial T}{\partial x} = G(x, \eta_{Abs}, P_L) = \frac{\eta_{Abs} \cdot P_L}{2 \cdot \pi \cdot \lambda_{th} \cdot x^2} \quad (7)$$

at the distance  $x$  behind the point source in the scan direction (positive  $x$ -direction).

Inserting Equation (6) in Equation (7), this temperature gradient is found to be

$$G_{x_{sol}}(\eta_{Abs}, P_L) = \frac{\eta_{Abs} \cdot P_L}{2 \cdot \pi \cdot \lambda_{th} \cdot \left(-\frac{\eta_{Abs} \cdot P_L}{2 \cdot \pi \cdot \lambda_{th} \cdot (T_{sol} - T_{amb})}\right)^2} = 2 \cdot \pi \cdot \lambda_{th} \cdot (T_{sol} - T_{amb})^2 \cdot \frac{1}{\eta_{Abs} \cdot P_L} \quad (8)$$

at the position of solidification  $x_{sol}$ .

Multiplication of Equation (8) with the scan velocity  $v$  results in the cooling rate

$$-\dot{T}_{sol}(v, \eta_{Abs}, P_L) = G_{x_{sol}}(\eta_{Abs}, P_L) \cdot v = 2 \cdot \pi \cdot \lambda_{th} \cdot (T_{sol} - T_{amb})^2 \cdot \frac{v}{\eta_{Abs} \cdot P_L} \quad (9)$$

at the position of solidification  $x_{sol}$  in the centre of the bead. Hence, the cooling rate  $-\dot{T}_{sol}$  during solidification is proportional to the scan velocity  $v$  and the inverse of the absorbed laser power  $\eta_{Abs} \cdot P_L$ .

By inserting Equation (9) in Equation (4), it follows that the Vickers hardness

$$HV(v, \eta_{Abs}, P_L) = k \cdot \left( \sigma_0 + \frac{C_{fit}}{\sqrt{K_{HP} \cdot (2 \cdot \pi \cdot \lambda_{th} \cdot (T_{sol} - T_{amb})^2 \cdot \frac{v}{\eta_{Abs} \cdot P_L})^{-n}}} \right) \quad (10)$$

can be expressed as a function of the process parameters scan velocity  $v$  and absorbed laser power  $\eta_{Abs} \cdot P_L$ .

### 3. Materials and Methods

AlSi10Mg, with a distribution of the size of the powder particles between 20 and 56  $\mu\text{m}$  [33], was used for the experiments. The material properties are listed in Table 1.

**Table 1.** Material properties used for AlSi10Mg [34,35].

$c_P$ in $\frac{\text{J}}{\text{kg} \cdot \text{K}}$	$\rho$ in $\frac{\text{kg}}{\text{m}^3}$	$\lambda_{th}$ in $\frac{\text{W}}{\text{m} \cdot \text{K}}$	$\kappa = \frac{\lambda_{th}}{\rho \cdot c_P}$ in $\frac{\text{m}^2}{\text{s}}$	$T_{sol}$ in $^\circ\text{C}$
910	2680	140–170	$5.74\text{--}6.97 \cdot 10^{-5}$	550–600

The samples used for the analysis of the hardness were generated with an industrial LPBF-machine TruPrint3000 from TRUMPF Laser- und Systemtechnik GmbH (Johann-Maus-Straße 2, Ditzingen, Germany). A modified substrate plate was used providing multiple boreholes for screws. The screws were used to fix aluminum sheets, which served as the substrates, on which the samples were generated. This allowed for simple and quick removal of the produced samples. Figure 1 illustrates the generation of the samples, with the first layer on a support structure (left) and with  $n$  layers after the processing time  $t$  (right). The support structure was implemented to ensure commonly used conditions as the majority of the manufactured parts are built on top of support structures. The processing space in the closed machine was continuously flushed with nitrogen as a shielding gas with a maximum of 0.3% oxygen [33,36]. The substrate temperature was set to  $T_{amb} = 200$  °C. The parts were generated on top of standardized support structures of the type “block” supplied by TRUMPF with a height of 5 mm and a line distance of the supports of 1 mm.

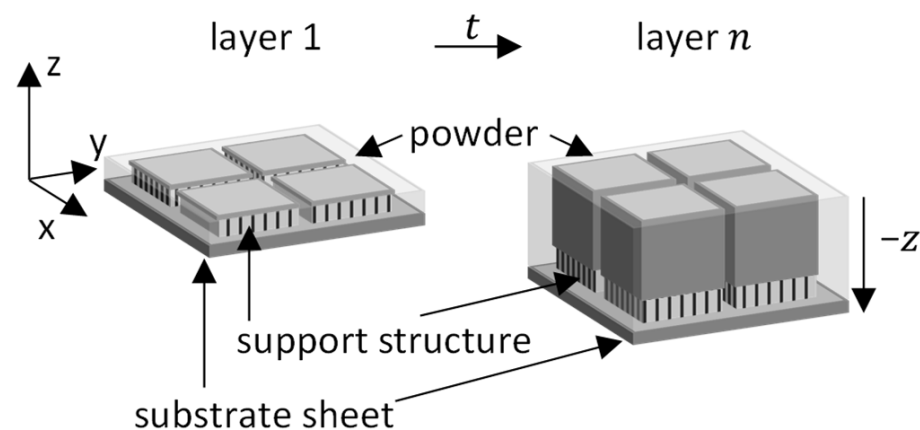


**Figure 1.** Illustration of the samples produced on removable substrate sheets.

Cubes with an edge length of 10 mm were generated for the present investigation. The height of the applied powder layers was set to 60  $\mu\text{m}$ . The layers were molten, using the chess hatch with zig-zag vectors with a hatch distance of 210  $\mu\text{m}$  for all experiments. The chess pattern was shifted by 4.02 mm in the x-direction and by 5.44 mm in the y-direction for each new layer to reduce the directionality of the sample. The vectors inside the pattern were either parallel or perpendicular to the contour of the cube, as shown in Figure 2.

Table 2 lists the applied parameters. The values of the absorptance  $\eta_{Abs}$  were taken from Leis et al. [21], as the absorptance is influenced by the incident laser power  $P_L$  and the diameter  $d_b$  of the beam on the surface of the sample. The experiments were performed within the optimum process window  $2000 \text{ W/mm} < \frac{P_L}{d_b} < 5200 \text{ W/mm}$  for AlSi10Mg [24] and with Péclet numbers smaller than  $Pe = (d_b \cdot v) / \kappa \leq 16 / \pi$  to match the case of three-dimensional heat flow [22–24], ensuring that the temperature distribution could be approximated by Equation (5). The parameters were selected in such a way that the aforementioned requirements were met and the parts could be produced using TruPrint3000.

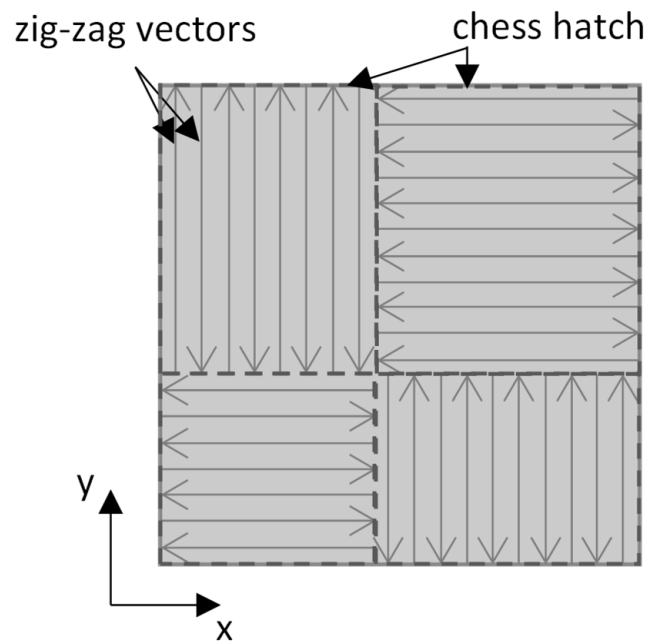


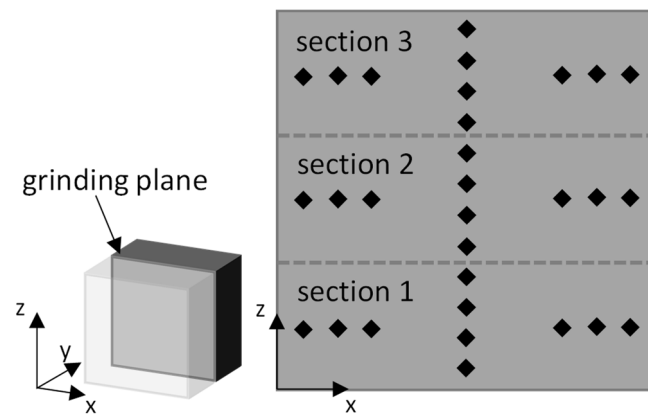
**Figure 2.** A single layer during the generation of the cube. The beam path vectors inside of the patterns are either perpendicular or parallel to the contour.

**Table 2.** Process parameters used to generate the cubic samples. The values of the absorptance  $\eta_{Abs}$  were taken from [21].

$\eta_{Abs}$ in 1 [21] $\pm 5\%$	$P_L$ in W	$d_b$ in $\mu\text{m}$	$P_L/d_b$ in W/mm	$v$ in mm/s	$Pe$ in 1 ( $\lambda_{th}=150 \frac{\text{W}}{\text{m}\cdot\text{K}}$ )
0.46	250	100	2500	1000	1.63
0.46	450	200	2250	1500	4.88
0.46	450	200	2250	750	2.44
0.46	450	200	2250	1000	3.25
0.46	250	100	2500	600	0.98
0.53	420	100	4200	1300	2.11
0.46	450	200	2250	500	1.63
0.46	250	100	2500	200	0.33
0.54	450	100	4500	750	1.22
0.46	450	200	2250	250	0.81
0.54	450	100	4500	500	0.81
0.51	350	100	3500	200	0.33
0.54	450	100	4500	200	0.33

The hardness values of the generated samples were determined according to Vickers in the small force range of HV0.5 in  $\text{N}/\text{mm}^2$ .

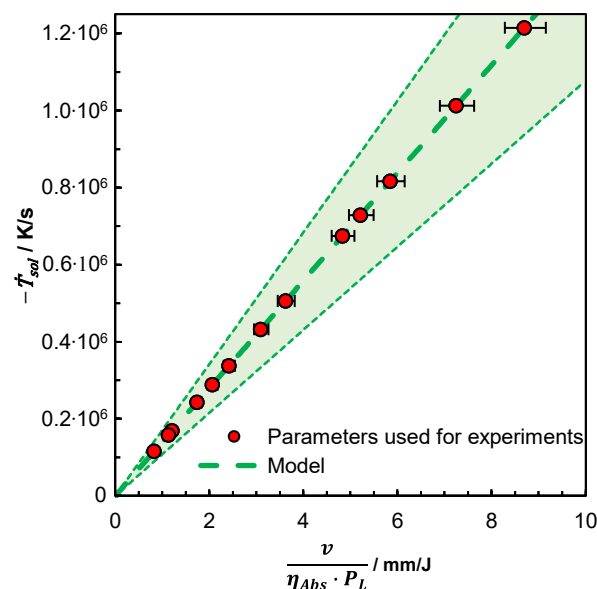
The hardness of the generated samples was measured with a Carat 930 from ATM GmbH. The samples were ground to the center and then stepwise polished down to a diamond suspension of  $3 \mu\text{m}$  before the hardness was measured. The hardness was measured at 30 different positions, as shown in Figure 3. This allowed the investigation of the influence of building height (sections 1, 2, and 3). Three samples were produced and characterized for each set of parameters.



**Figure 3.** Illustration of the measurement positions to determine the hardness at different locations in the samples.

#### 4. Results and Discussion

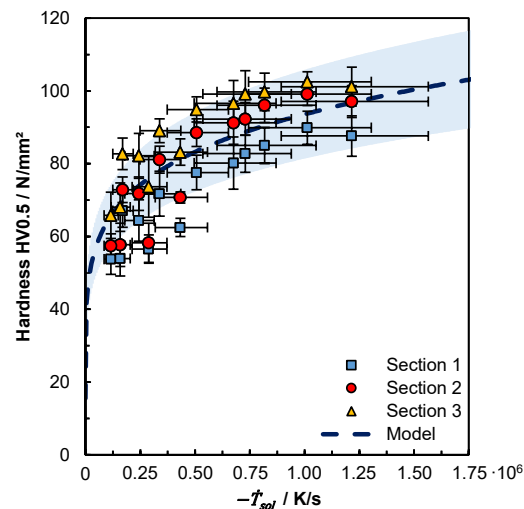
Figure 4 shows the cooling rates  $-\dot{T}_{sol}$  as a function of the process parameters, according to Equation (9). The green dashed line represents the cooling rates assuming  $\lambda_{th} = 150 \frac{W}{m \cdot K}$  and  $T_{sol} = 585 \text{ } ^\circ\text{C}$ . The upper dotted line results when assuming  $\lambda_{th} = 170 \frac{W}{m \cdot K}$  and  $T_{sol} = 600 \text{ } ^\circ\text{C}$ , and the lower dotted line corresponds to  $\lambda_{th} = 140 \frac{W}{m \cdot K}$  and  $T_{sol} = 550 \text{ } ^\circ\text{C}$ . Therefore, the green shaded area represents the uncertainty on the cooling rates  $\dot{T}_{sol}$  due to the variable material properties of AlSi10Mg, which are shown in Table 1. This variation in material properties may be due to batch-dependent varying contents of alloying elements, even when they are still within the standardized material definition. For example, the silicon content may vary between 9 and 11 wt.%, which influences melting temperatures [37]. The same ranges will also be considered in the following discussion. The red dots mark the calculated cooling rates resulting from the applied process parameters listed in Table 2, assuming  $\lambda_{th} = 150 \frac{W}{m \cdot K}$  and  $T_{sol} = 585 \text{ } ^\circ\text{C}$ . The horizontal error bars stem from the possible variation of the absorptance  $\eta_{Abs} \pm 5 \%$ .



**Figure 4.** Cooling rate according to Equation (9). The green shaded area illustrates the uncertainty due to variations of the material (see text). The dots show the parameters used to prepare the samples.

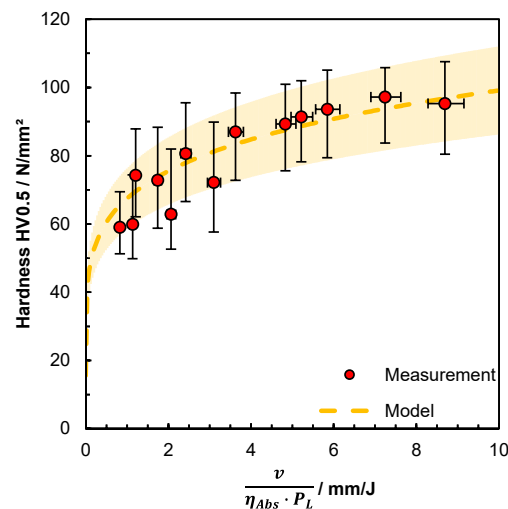
The blue dashed line in Figure 5 shows the hardness according to Equation (4) using the quantities mentioned above,  $C_{fit} = 170 \frac{N \cdot \sqrt{\mu\text{m}}}{\text{mm}^2}$ ,  $\lambda_{th} = 150 \frac{W}{m \cdot K}$ ,  $T_{sol} = 585 \text{ } ^\circ\text{C}$ , and  $k = 2.615^{-1}$ . The dots show the hardness values measured in the different sections (cf.

Figure 4), where the cooling rate was calculated with Equation (9) using the same values as for the blue dashed line. The light blue shaded area represents the uncertainty resulting from the variable material properties of AlSi10Mg listed in Table 1, an uncertainty of  $C_{fit} = 170 \pm 10 \frac{N \cdot \sqrt{\mu m}}{mm^2}$ , and the range of  $k = (2.615 \pm 0.125)^{-1}$ . The vertical error bars of the measurements show the standard deviation of the 30 hardness values measured in the same section on three samples. The horizontal error bars of the measurements show the uncertainty resulting from the variable material properties of AlSi10Mg listed in Table 1, an uncertainty of  $C_{fit} = 170 \pm 10 \frac{N \cdot \sqrt{\mu m}}{mm^2}$ , and the range of  $k = (2.615 \pm 0.125)^{-1}$ . Notably, the hardness of the upper section 3 (further away from the support structure) is higher than the one of the lower sections (closer to the support structure). This influence is diminishing with increasing distance from the support structure (the difference between section 2 and section 3 is smaller than the difference between section 1 and section 2). Due to the proximity of section 1 to the support structures, lower cooling rates are expected compared to the ones assumed in the model, which is also reflected by the lower hardness in the experimental results. Despite this low dependence, the majority of the measured hardness values are within the blue shaded band predicted by the proposed theoretical model.



**Figure 5.** Hardness in HV0.5 as a function of the calculated cooling rate. The blue dashed line corresponds to Equation (4). The uncertainty due to the variable material properties is represented by the blue shaded area. The points show the experimentally measured hardness averaged over 30 measurements, where the cooling rate was calculated using Equation (9). The height of the error bars shows the standard deviation of the measurements; the length of the error bars in horizontal direction shows the uncertainty due to the variable material properties.

The orange dashed line in Figure 6 corresponds to the proposed model given by Equation (10) with  $\lambda_{th} = 150 \frac{W}{m \cdot K}$ ,  $T_{sol} = 585 \text{ } ^\circ\text{C}$ ,  $C_{fit} = 170 \frac{N \cdot \sqrt{\mu m}}{mm^2}$ , and  $k = 2.615$ . The light orange shaded area indicates the same material-related uncertainty as mentioned above. The red dots show the hardness as an average across all measurements in the three sections, and over the three samples produced with the same process parameters. The error bars of the hardness are again given by the standard deviation. The horizontal error bars take into account the possible variation of the absorptance  $\eta_{Abs} \pm 5 \%$ . The results show an excellent agreement between the proposed model and the experimental findings.



**Figure 6.** Hardness in HV0.5 as a function of the process parameters. The yellow dashed line corresponds to the proposed model given by Equation (10). The uncertainty due to the variable material properties is represented by the light orange shaded area. The points show the experimentally measured hardness averaged over 90 measurements in the three sections. The height of the vertical error bars shows the minimum and maximum values of the standard deviation, which are shown in Figure 5. The error bars in  $x$ -direction show the possible variation of the absorptance  $\eta_{Abs} \pm 5\%$  as shown in Table 2.

## 5. Conclusions

This study demonstrates that the hardness of LPBF parts of AlSi10Mg can be tuned by adjusting the scan velocity  $v$  and absorbed laser power  $\eta_{Abs} \cdot P_L$ . The agreement between the derived model and the experimental results is very high, which eliminates the need for elaborate material analyses, such as electron backscatter diffraction (EBSD) and other characterizations, to predict the mechanical properties. This confirms that the approach of modeling the LPBF process based on the three-dimensional heat-conduction equation with a moving point source is viable. Within the optimum process window, this knowledge makes it possible to tune the hardness of additively manufactured parts of AlSi10Mg in a range between 60 HV0.5 and 100 HV0.5 for  $T_{amb} = 200$  °C simply by adjusting the cooling rate during solidification with an appropriate choice of the processing parameters.

Future work will be devoted to the application of the derived model on complex parts and other materials suitable for LPBF.

**Author Contributions:** Conceptualization, A.L.; investigation, A.L. and D.T.; writing—original draft preparation, A.L.; writing—review and editing, D.T., R.W. and T.G. All authors have read and agreed to the published version of the manuscript.

**Funding:** This research was funded by the Deutsche Forschungsgemeinschaft (DFG, German Research Foundation) within the framework of the Excellence Initiative—GSC 262.

**Data Availability Statement:** Data is contained within the article.

**Acknowledgments:** The authors would like to thank TRUMPF Laser- und Systemtechnik GmbH + Co. KG for supplying the TruPrint3000 at the research campus ARENA 2036 for manufacturing the samples and performing the experiments.

**Conflicts of Interest:** The authors declare no conflict of interest. The funders had no role in the design of the study; in the collection, analyses, or interpretation of data; in the writing of the manuscript, or in the decision to publish the results.

## References

1. Ravalji, J.M.; Raval, S.J. Review of quality issues and mitigation strategies for metal powder bed fusion. *Rapid Prototyp. J.* 2022; *ahead-of-print*. [CrossRef]
2. Zhou, Y.; Abbara, E.M.; Jiang, D.; Azizi, A.; Poliks, M.D.; Ning, F. High-cycle fatigue properties of curved-surface AlSi10Mg parts fabricated by powder bed fusion additive manufacturing. *Rapid Prototyp. J.* 2022, 28, 1346–1360. [CrossRef]
3. Wang, D.; Wei, X.; Liu, J.; Xiao, Y.; Yang, Y.; Liu, L.; Tan, C.; Yang, X.; Han, C. Lightweight design of an AlSi10Mg aviation control stick additively manufactured by laser powder bed fusion. *Rapid Prototyp. J.* 2022, 28, 1869–1881. [CrossRef]
4. Wang, D.; Liu, L.; Deng, G.; Deng, C.; Bai, Y.; Yang, Y.; Wu, W.; Chen, J.; Liu, Y.; Wang, Y.; et al. Recent progress on additive manufacturing of multi-material structures with laser powder bed fusion. *Virtual Phys. Prototyp.* 2022, 17, 329–365. [CrossRef]
5. Takata, N.; Kodaira, H.; Sekizawa, K.; Suzuki, A.; Kobashi, M. Change in microstructure of selectively laser melted AlSi10Mg alloy with heat treatments. *Mater. Sci. Eng. A* 2017, 704, 218–228. [CrossRef]
6. Sajadi, F.; Tiemann, J.-M.; Bandari, N.; Darabi, A.C.; Mola, J.; Schmauder, S. Fatigue Improvement of AlSi10Mg Fabricated by Laser-Based Powder Bed Fusion through Heat Treatment. *Metals* 2021, 11, 683. [CrossRef]
7. Matyja, H.; Giessen, B.C.; Grant, N.J. The Effect of cooling Rate on the Dendrite Spacing in Splat-Cooled Aluminum Alloys. *J. Inst. Met.* 1968, 1968, 30–32.
8. Gandolfi, M.; Xavier, M.; Gomes, L.; Reyes, R.; Garcia, A.; Spinelli, J. Relationship between Microstructure Evolution and Tensile Properties of AlSi10Mg Alloys with Varying Mg Content and Solidification Cooling Rates. *Metals* 2021, 11, 1019. [CrossRef]
9. Hall, E.O. The Deformation and Ageing of Mild Steel: III Discussion of Results. *Proc. Phys. Soc. Sect. B* 1951, 64, 747–753. [CrossRef]
10. Köster, W.; Altenpohl, D. *Aluminium und Aluminiumlegierungen*; Springer Berlin Heidelberg: Berlin/Heidelberg, Germany, 1965; ISBN 978-3-662-30246-0.
11. Khodabakhshi, F.; Haghshenas, M.; Eskandari, H.; Koohbor, B. Hardness–strength relationships in fine and ultra-fine grained metals processed through constrained groove pressing. *Mater. Sci. Eng. A* 2015, 636, 331–339. [CrossRef]
12. Boschetto, A.; Costanza, G.; Quadrini, F.; Tata, M. Cooling rate inference in aluminum alloy squeeze casting. *Mater. Lett.* 2007, 61, 2969–2972. [CrossRef]
13. Cerri, E.; Ghio, E. AlSi10Mg Alloy Produced by Selective Laser Melting: Relationships between Vickers Microhardness, Rockwell Hardness and Mechanical Properties. *Int. J. Ital. Assoc. Metall.* 2020, 5–17. Available online: [http://www.aimnet.it/la\\_metallurgia\\_italiana/2020/lug-ago/cerri.pdf](http://www.aimnet.it/la_metallurgia_italiana/2020/lug-ago/cerri.pdf) (accessed on 29 March 2022).
14. Wei, F.; Cheng, B.; Chew, L.T.; Lee, J.J.; Cheong, K.H.; Wu, J.; Zhu, Q.; Tan, C.C. Grain distribution characteristics and effect of diverse size distribution on the Hall–Petch relationship for additively manufactured metal alloys. *J. Mater. Res. Technol.* 2022, 20, 4130–4136. [CrossRef]
15. Esmaeilzadeh, R.; Keshavarzkermani, A.; Ali, U.; Mahmoodkhani, Y.; Behraves, B.; Jahed, H.; Bonakdar, A.; Toyserkani, E. Customizing mechanical properties of additively manufactured Hastelloy X parts by adjusting laser scanning speed. *J. Alloys Compd.* 2019, 812, 152097. [CrossRef]
16. Simonds, B.; Sowards, J.; Hadler, J.; Pfeif, E.; Wilthan, B.; Tanner, J.; Harris, C.; Williams, P.; Lehman, J. Dynamic and absolute measurements of laser coupling efficiency during laser spot welds. *Procedia CIRP* 2018, 74, 632–635. [CrossRef]
17. Trapp, J.; Rubenchik, A.M.; Guss, G.; Matthews, M.J. In situ absorptivity measurements of metallic powders during laser powder-bed fusion additive manufacturing. *Appl. Mater. Today* 2017, 9, 341–349. [CrossRef]
18. Khorasani, M.; Ghasemi, A.; Leary, M.; Sharabian, E.; Cordova, L.; Gibson, I.; Downing, D.; Bateman, S.; Brandt, M.; Rolfe, B. The effect of absorption ratio on meltpool features in laser-based powder bed fusion of IN718. *Opt. Laser Technol.* 2022, 153, 108263. [CrossRef]
19. Tenbrock, C.; Fischer, F.G.; Wissenbach, K.; Schleifenbaum, J.H.; Wagenblast, P.; Meiners, W.; Wagner, J. Influence of keyhole and conduction mode melting for top-hat shaped beam profiles in laser powder bed fusion. *J. Mater. Process. Technol.* 2019, 278, 116514. [CrossRef]
20. Patel, S.; Vlasea, M. Melting modes in laser powder bed fusion. *Materialia* 2020, 9, 100591. [CrossRef]
21. Leis, A.; Weber, R.; Graf, T. Influence of the process parameters on the absorptance during Laser-Based Powder Bed Fusion of AlSi10Mg. *Procedia CIRP* 2020, 94, 173–176. [CrossRef]
22. Arata, Y.; Maruo, H.; Miyamoto, I. *Application of Laser for Material Processing-Heat Flow in Laser Hardening*; IIW: Genoa, Italy, 1978.
23. Graf, T.; Berger, P.; Weber, R.; Hügel, H.; Heider, A.; Stritt, P. Analytical expressions for the threshold of deep-penetration laser welding. *Laser Phys. Lett.* 2015, 12, 56002. [CrossRef]
24. Leis, A.; Weber, R.; Graf, T. Process Window for Highly Efficient Laser-Based Powder Bed Fusion of AlSi10Mg with Reduced Pore Formation. *Materials* 2021, 14, 5255. [CrossRef] [PubMed]
25. Shanmugasundaram, T.; Heilmaier, M.; Murty, B.; Sarma, V.S. On the Hall–Petch relationship in a nanostructured Al–Cu alloy. *Mater. Sci. Eng. A* 2010, 527, 7821–7825. [CrossRef]
26. Choi, H.; Lee, S.; Park, J.; Bae, D. Tensile behavior of bulk nanocrystalline aluminum synthesized by hot extrusion of ball-milled powders. *Scr. Mater.* 2008, 59, 1123–1126. [CrossRef]
27. Mukai, T.; Ishikawa, K.; Higashi, K. Influence of strain rate on the mechanical properties in fine-grained aluminum alloys. *Mater. Sci. Eng. A* 1995, 204, 12–18. [CrossRef]

28. Hayes, R.; Witkin, D.; Zhou, F.; Lavernia, E.J. Deformation and activation volumes of cryomilled ultrafine-grained aluminum. *Acta Mater.* **2004**, *52*, 4259–4271. [[CrossRef](#)]
29. Hyer, H.; Zhou, L.; Park, S.; Gottsfritz, G.; Benson, G.; Tolentino, B.; McWilliams, B.; Cho, K.; Sohn, Y. Understanding the Laser Powder Bed Fusion of AlSi10Mg Alloy. *Met. Microstruct. Anal.* **2020**, *9*, 484–502. [[CrossRef](#)]
30. Tang, M.; Pistorius, P.C.; Narra, S.P.; Beuth, J.L. Rapid Solidification: Selective Laser Melting of AlSi10Mg. *JOM* **2016**, *68*, 960–966. [[CrossRef](#)]
31. Rykalin, N.N. *Die Wärmegrundlagen des Schweißvorganges die Wärmeaustauschvorgänge bei der Lichtbogenschweißung*; Verl. Technik: Berlin, Germany, 1952.
32. Rosenthal, D. The theory of moving sources of heat and its application to metal treatments. *Trans. ASME* **1946**, *86*, 849–866.
33. TRUMPF Laser- und Systemtechnik GmbH. *TRUMPF Additive Manufacturing: Batch Test Report. Aluminium AlSi10Mg-A LMF—Results Reference Process*; TRUMPF Laser- und Systemtechnik GmbH: Ditzingen, Germany, 2019.
34. Raffmetal, S.p.a. Leghe di Alluminio in Colata. Continuous Casting Aluminium Alloys: AlSi10Mg. Available online: [http://www.raffmetal.com/scarica\\_file.asp?c=/dati/SearchAlloy/ENG/&f=EN43000.pdf](http://www.raffmetal.com/scarica_file.asp?c=/dati/SearchAlloy/ENG/&f=EN43000.pdf) (accessed on 18 February 2020).
35. Nogowizin, B. *Theorie und Praxis des Druckgusses*; Schiele & Schön: Berlin, Germany, 2011; ISBN 9783794907960.
36. EOS GmbH. EOS Aluminium AlSi10Mg: Material Data Sheet. Metal Solutions. Available online: [https://www.eos.info/03\\_system-related-assets/material-related-content/metal-materials-and-examples/metal-material-datasheet/aluminium/material-datasheet\\_eos\\_aluminium-alsi10mg\\_en\\_web.pdf](https://www.eos.info/03_system-related-assets/material-related-content/metal-materials-and-examples/metal-material-datasheet/aluminium/material-datasheet_eos_aluminium-alsi10mg_en_web.pdf) (accessed on 2 August 2021).
37. DIN Deutsches Institut für Normung e.V. *Aluminium und Aluminiumlegierungen—Gussstücke: Chemische Zusammensetzung und mechanische Eigenschaften*; Deutsche Fassung EN 1706:2020+A1:2021, ICS 77.150.10(DIN EN 1706); Beuth Verlag GmbH: Berlin, Germany, 2021.